Physical Modeling: Simulation of Micro-Void Development within Large Scale Polymer Composite Deposition Beads

Aigbe Awenlimobor [1*], Zhaogui Wang [2], Douglas E. Smith[1]

[1]Department of Mechanical Engineering, School of Engineering and Computer Science, Baylor University, Waco, TX 76798, USA

[2]Department of Mechanical Engineering, Naval Architecture and Ocean Engineering College, Dalian Maritime University, Dalian 116000, China

*Corresponding author. Email: aigbe_awenlimobor1@baylor.edu

Abstract

Short carbon fiber composites are used in large-scale polymer deposition additive manufacturing due to their increased stiffness and strength and reduced thermal expansion and print distortion. While much attention has been given to interlayer properties, less is known about bead microstructure, including the effect that suspended fibers have on porosity. This paper develops a model for single fiber motion in a purely viscous flow that is simulated with a custom finite element fiber suspension analysis. Our fiber simulation is based on Jeffrey's model assumptions where translational and rotational velocities which zero applied forces and moments are computed. Velocity gradients along streamlines within the flow of polymer melt through a large-scale polymer deposition additive manufacturing flow field serve as input. The pressure distribution around a fiber is computed along the flow path including the die swell expansion at the nozzle exit. The simulation provides insight into micro-void formation within printed beads.

Introduction

Among various Additive Manufacturing (AM) techniques such as Selective Laser Sintering (SLS) and Stereolithography (SLA), Fused Filament Fabrication (FFF) is a fast-growing technique which deposits polymer and polymer composite beads enabling rapid prototyping and extensive design freedom at no additional cost [1]. Research on bead microstructure formed during large-scale polymer composite deposition has gained widespread attention due to the significant impact short carbon fibers have on the physical and thermomechanical properties of the composite parts [2]. Among other microstructural properties of interest including fiber orientation and fiber volume fraction, micro-voids formed in the manufacturing process remain a concern since they negatively impact the stiffness, strength, quality, and cost of the components design, and pose severe risk of component failure under in-service loads [3]. There has been record of successful implementation of various computational methods such as work done by Heller et al. [4] and Wang et al. [5] in simulating the short fiber composite deposition process for Big Area Additive Manufacturing (BAAM) and evaluating microstructural properties such as fiber orientation and the resulting thermo-mechanical properties. However, little progress has been made in understanding the formation and evolution of micro-voids, including the role played by the suspended fibers in their development. Vaxman et al. [6] suggest that voids nucleate at fiber ends and the process begins when air is entrapped in polymer melt during compounding and processing stages. They also show that the fiber volume fraction directly affects the viscosity of the polymer melt which influences void formation in prints together with other factors such as the shear rate, flow temperature, and fiber's aspect ratio. The difference in the fiber-matrix thermal expansion coefficient, the die swell/expansion of the free extrudate and differential cooling rate between the bead's external surface and core regions are contributing factors that also increase porosity. Yang et al. [7] showed that void percentage is negligible during the filament feed

and melt stages within the extruder and nozzle. They also showed that most voids form when polymer melt just exits nozzle and that this percentage drops during on-bed deposition due to air escapement.

The aim of this paper is not to predict void formation but to better understand mechanisms that promote void formation within beads produced by BAAM polymer composite deposition. Our hypothesis is that voids nucleate in low pressure regions along the fiber surface during the deposition process. Here we present a multiscale modelling approach to achieve our objective: first we develop a macro scale-2D planar deposition flow model for fiber orientation within the 2D polymer composite melt flow of the BAAM nozzle which is used to predict the flow field and fiber orientation tensors in the nozzle. Secondly, we develop a micro scale model to simulate the motion of a single ellipsoidal fiber suspended in a polymeric melt flow using the computed velocity and pressure from the macro scale model as inputs for the microscale model. The micro model is based on the work by Zhang et al. [10] which incorporates Jeffrey's [8] assumptions for suspended particles. In this approach, we compute the fiber's linear and angular velocities that result in zero net hydrodynamic forces and torques and subsequently determine the fiber evolution using an explicit numerical algorithm to track its position and orientation. The resulting pressure distribution around the fiber along the flow path, including the die swell expansion at the nozzle outlet provides insight into the micro-void formation mechanism within printed beads. We validate the modeling approach by benchmarking results for a shear flow with analytical solutions developed by Jeffery [8]. The simulation approach presented here is expected to provide unique insight into microstructure development during BAAM processing which can be used to improve the quality of manufactured composite parts.

Methodology

We consider the following multiscale modelling approach:

1. A Macro scale model is used to compute the velocity and pressure solution along streamlines within a 2D polymer composite melt flow of the BAAM nozzle. Fiber orientation tensors are then computed along each streamline from the velocity solution.
2. A Micro model is used to simulates the motion of a single ellipsoidal fiber suspended and compute the pressure field near a fiber in a polymeric melt flow using inputs from the velocity streamlines from the macroscale model as boundary conditions.

Macro Model - 2D Planar Deposition Flow

In the macro model [9], we compute the velocity flow field within the 2D planar flow of a BAAM nozzle (cf. Figure 1) using ANSYS Polyflow software. The fiber presence is ignored during the flow computation. The polymer melts in the barrel and is forced through the nozzle and extruded onto the moving plate or predeposited material below (relative to the nozzle). The relevant polymer melt properties used in this study are for 13% carbon fiber filled ABS evaluated for a shear rate of 100 s^{-1} at 230°C where the density is $1154\ kgm^3$ and the viscosity is $817 Pa \cdot s$.
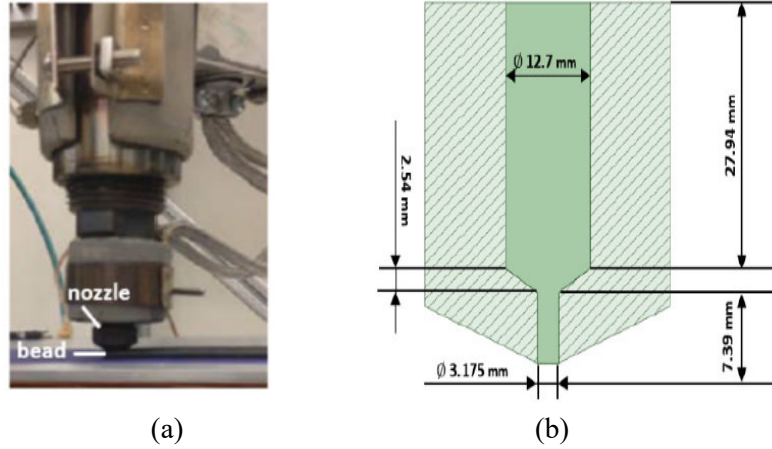
Figure 1: a) Polymer Deposition Process, b) Extrusion Die Schematic. [9]

The governing equations based on the assumption of incompressible, isothermal, viscous, low Reynolds number, and Newtonian fluid flow are the Stokes equation for mass and momentum conservation of the polymer melt flow given as

$$\nabla \cdot \boldsymbol{u} = 0 \tag{1}$$

$$\nabla \cdot \boldsymbol{\sigma} + \boldsymbol{f} = 0 \tag{2}$$

where $\boldsymbol{u}$ is the flow velocity vector, $\boldsymbol{f}$ is the body force vector and $\boldsymbol{\sigma}$ is the Cauchy stress tensor given as

$$\boldsymbol{\sigma} = \boldsymbol{\tau} - p\boldsymbol{I} \tag{3}$$

In the above, p is the fluid hydrostatic pressure, $\boldsymbol{I}$ is the identity tensor and $\boldsymbol{\tau}$ is the deviatoric stress tensor given as

$$\boldsymbol{\tau} = 2\mu\boldsymbol{D} \tag{4}$$

where μ is the viscosity of the Newtonian fluid, and $\boldsymbol{D}$ is the second-order rate of deformation tensor.

The two-dimensional (2D) planar deposition flow domain consists of the extrusion nozzle's hollow section and a single bead layer deposited on the moving bed with the relevant prescribed boundary conditions as shown in Figure 2.
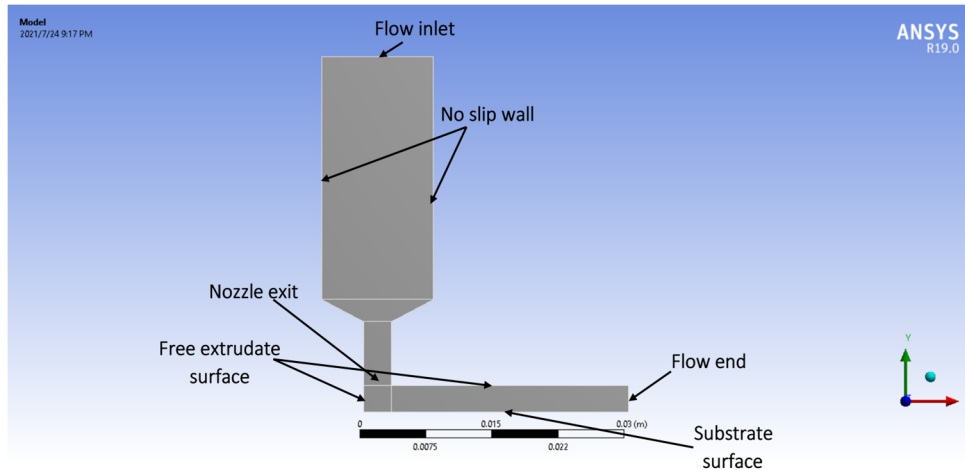
Figure 2: 2D Planar deposition flow model with relevant boundary conditions

The computed velocity contours and streamlines from the macro scale simulation appear in Figure 3. Of particular interest are streamlines 10, 15 and 18 with deposition times of 1.112, 1.487, and 2.780 seconds, respectively, which serve as basis for the microscale analysis. The velocity contours are characterized by sharp transitions of velocity gradient as the polymer exits the nozzle. Within the extruder itself, the transverse velocity variation across the width is nearly linear, but the longitudinal velocity is seen to increase significantly towards the center and downstream towards the nozzle.
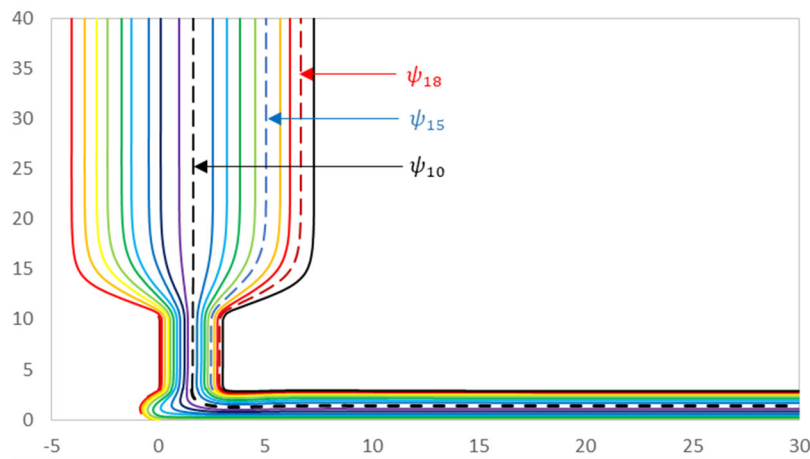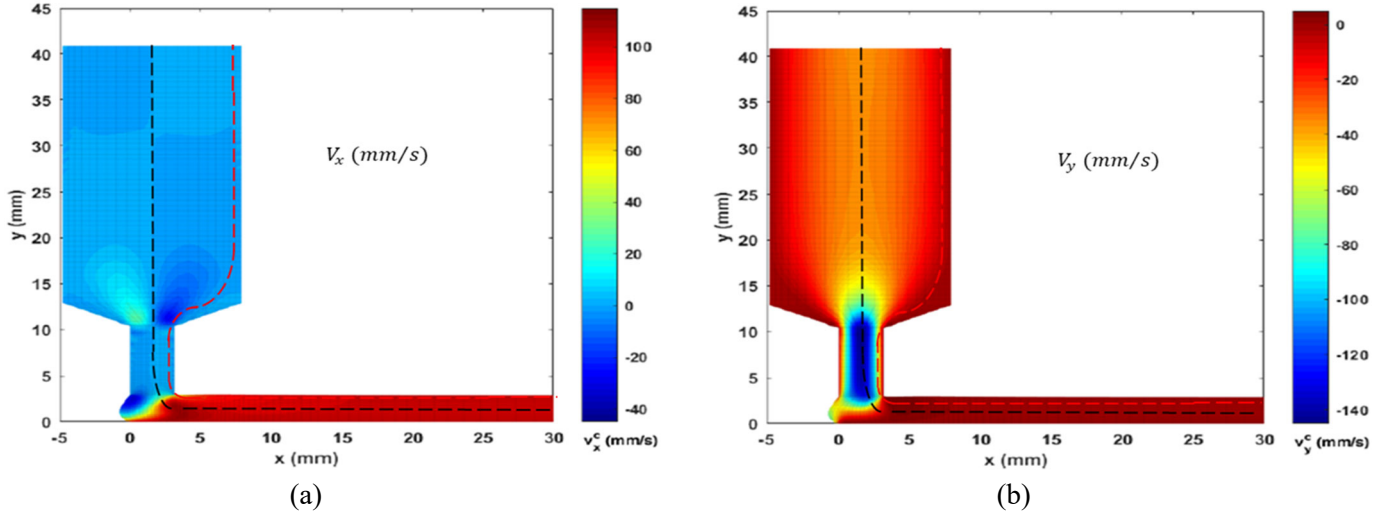

Figure 3: Velocity Streamlines – fully coupled solution

Figure 4: Velocity contours a) horizontal velocity v_x b) vertical velocity v_y

Micro-Model – 2D Single Fiber Evolution Model

Our micro model is based on the work of Zhang et al. [10] using a custom finite element analysis (FEA) code written in MATLAB to simulate the motion of a single ellipsoidal fiber in the polymeric melt flow. Inputs to the micro model include velocity, velocity gradients, and pressure which are computed in the macroscale model as described in the preceding section. The equation governing the model development are the same Stokes's equation utilized in the macro-model based on similar assumptions of steady state, incompressible, low Reynolds number, isothermal flow with an isotropic, homogenous, symmetric, and Newtonian fluid property. The micro model assumes a no slip boundary condition at fluid and fiber interface and no flux through the fiber surface. The micro model has the same polymer melt properties as the macro model.

In the micro model FEA code, we assemble each element stiffness matrix derived from the Galerkin formulations of the governing equations (cf. Equations 1-4) into a global system and solve for unknown nodal velocities, pressures, and nodal reactions. Using the FEA algorithm, we iteratively determine the fiber's translational and angular velocities based on a Newton Raphson's algorithm that zero's the net hydrodynamic force and torque acting on the fiber's surface due to the action of the surrounding fluid. In this computational approach, the fiber's evolution (translation and rotation) is computed at each time step using an explicit 4th order Runge-Kutta scheme.

We consider 3 prescribed essential boundary conditions for primary variable $\bar{u}$ [10] & [11]. as shown in Figure 5.

BC 1: The far-field velocity at the fluid boundary U_{BC3}, which are derived from the velocity profiles and gradients of the streamline obtained from the macro-model are implemented as (where Δx and Δy are the distance from the fiber center to the far-field boundary at each node)

$$U_{BC1} = \underline{U'_0} = \begin{bmatrix} u_\psi \\ v_\psi \end{bmatrix} + \begin{bmatrix} \partial u_\psi / \partial x & \partial u_\psi / \partial y \\ \partial v_\psi / \partial x & \partial v_\psi / \partial y \end{bmatrix} \begin{bmatrix} \Delta x \\ \Delta y \end{bmatrix} \qquad 5$$

BC 2: The fluid pressure constraint p_{BC2} is prescribed by imposing the far-field streamline pressure p'_0 on a node on the fluid surface according to Eqn. 6

$$p_{BC2} = p'_0 \qquad 6$$

BC 3: The velocity prescribed at the fiber's edge U_{BC3} is obtained from the equation of rigid body motion (Eqn. 7) and is comprised of the fiber's center velocity and the component of the relative motion of the fiber surface referenced to its center.

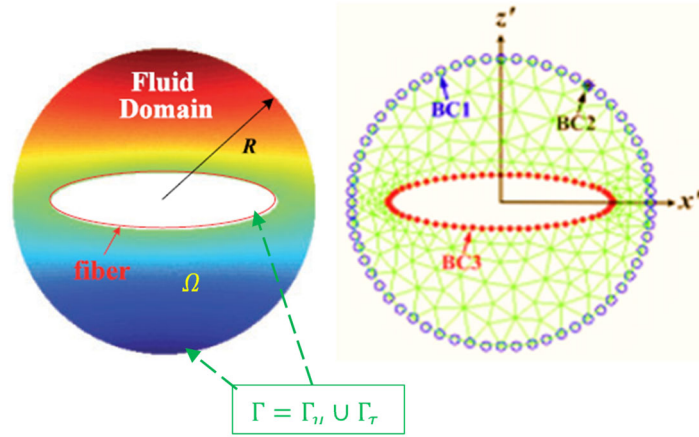$$U_{BC3} = \underline{U'_c} + \omega' \times \underline{r'} \qquad 7$$

Figure 5: Micro-model showing prescribed boundary conditions [10]

For the Finite Element model discretization, we use a radial seed of 13 cell units with a geometric radial bias of 1.2 and circumferential seed of 50 cell unit leading to a total of $2 \times 13 \times 25 = 650$ triangular elements as shown in Figure 6(a). A sensitivity analysis was performed to determine the sufficient number of elements such that our results accurately predict Jeffery's orbit (cf. Figure 7).
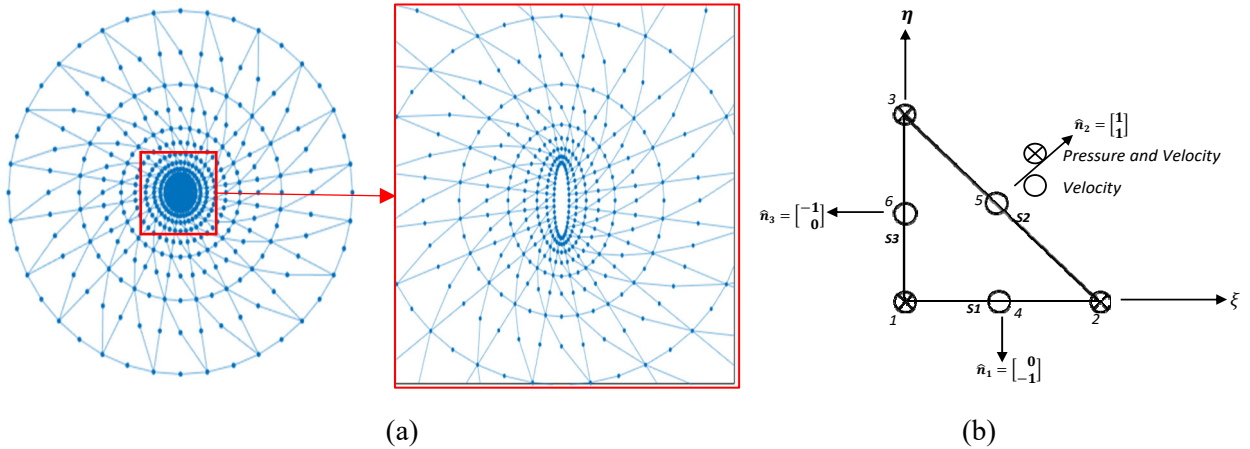

(a)   (b)

Figure 6: a) Fluid domain discretization b) Element type with velocity and pressure *DoF*

In the FEA formulation, we employ the mixed method approach with $(u, v, \& p)$ as the primary nodal variables. As shown in Figure 6 (b), a 6-node quadratic, iso-parametric triangle serendipity element, with three degrees of freedom at each corner node $(u, v, \& p)$ and two degrees of freedom at the mid-side nodes (u, v) is used which has been found to give accurate results for low Reynolds number fluid flow problems [13].

The discretized linear algebraic equations derived though the finite element formulation yields the system matrix equation

$$\underline{\underline{K}}\, \underline{U} = \underline{F} \qquad\qquad 8$$

where $\underline{\underline{K}}$ is the global system 'stiffness' matrix, $\underline{U}$ is the primary dependent variable vector containing the nodal velocities and pressures and $\underline{F}$ is the secondary variable vector containing the associated nodal reaction forces and flow rates. We partition the system matrices based on the essential (denoted by an $'e'$ post subscript) and free (denoted by an $'f'$ post subscript) degrees of freedom as

$$\begin{bmatrix} K_{ff} & K_{fe} \\ K_{ef} & K_{ee} \end{bmatrix} \begin{bmatrix} u_f \\ u_e \end{bmatrix} = \begin{bmatrix} F_f \\ F_e \end{bmatrix} \qquad\qquad 9$$

such that the unknown independent and dependent variables are computed from [10]

$$\underline{u}_f = \underline{\underline{K}}_{ff}^{-1} \left(\underline{F}_f - \underline{\underline{K}}_{fe}\underline{u}_e \right), \ \ \underline{F}_e = \underline{\underline{K}}_{ef}\underline{u}_f + \underline{\underline{K}}_{ee}\underline{u}_e \qquad\qquad 10$$

The resultant fiber's hydrodynamic force vector $\underline{F}_H$ and couple T_H due to the impingement of the surrounding fluid on the fiber's surface is computed by summing the nodal reactions force vectors and summing the cross product of the nodal position vectors and corresponding reaction force vectors over the fiber surface $(BC3)$, respectively, as

$$\underline{F}_H = -\sum_{n\in N} \underline{F}_{e,n}^{BC3}, \ \ T_H = -\sum_{n\in N} \underline{r}_n \times \underline{F}_{e,n}^{BC3} \qquad\qquad 11$$

where $\underline{r}_n$ and $\underline{F}_{e,n}^{BC3}$ are the position vector and nodal reaction force vectors at the nth node on the fiber's surface $(BC3)$, and N is the total number of nodes on the fibers surface. To obtain the fiber's translational and rotational velocities, the hydrodynamic forces and torque are zeroed using a Newton-Raphson (NR) iteration scheme written as [11]

$$\underline{X}^+ = \underline{X}^- - \underline{\underline{J}}^- \backslash \underline{R}^- \qquad\qquad 12$$

In the above, the residual vector $\underline{R}$ contains the fiber hydrodynamic forces $\underline{F}_H$ and couple T_H which are functions of the fiber's velocity vector $\underline{X}$ which in turn depends on the translational (u_c, v_c) and angular ω velocity components, i.e. $\underline{R} = \begin{bmatrix} \underline{F}_H(\underline{X}) & T_H(\underline{X}) \end{bmatrix}^T$ and $\underline{X} = \begin{bmatrix} u_c & v_c & \omega \end{bmatrix}^T$. The Jacobian $\underline{\underline{J}}$ is the derivative of the residual vector $\underline{R}$ with respect to the fiber's velocity vector $\underline{X}$ which may be written as

$$\underline{\underline{J}} = \frac{\partial \underline{R}}{\partial \underline{X}} = \begin{bmatrix} \dfrac{\partial \underline{F}_H}{\partial \underline{X}} \\[2mm] \dfrac{\partial T_H}{\partial \underline{X}} \end{bmatrix} = \begin{bmatrix} -\sum_{n\in N} \dfrac{\partial \underline{F}_{e,n}^{BC3}}{\partial \underline{X}} \\[4mm] -\sum_{n\in N} \underline{r}_n \times \dfrac{\partial \underline{F}_{e,n}^{BC3}}{\partial \underline{X}} \end{bmatrix} \qquad\qquad 13$$

The derivative of the nodal reaction force vector with respect to the fiber's velocity vector is given as

$$\frac{\partial \underline{F}_e}{\partial \underline{X}} = \frac{\partial \underline{\underline{K}}_{ef}}{\partial \underline{X}} \underline{u}_f + \underline{\underline{K}}_{ef} \frac{\partial \underline{u}_f}{\partial \underline{X}} + \frac{\partial \underline{\underline{K}}_{ee}}{\partial \underline{X}} \underline{u}_e + \underline{\underline{K}}_{ee} \frac{\partial \underline{u}_e}{\partial \underline{X}} \qquad 14$$

where:

$$\frac{\partial \underline{u}_f}{\partial \underline{X}} = \underline{\underline{K}}_{ff}^{-1} \left(\frac{\partial \underline{F}_f}{\partial \underline{X}} - \frac{\partial \underline{\underline{K}}_{ff}}{\partial \underline{X}} \underline{u}_f - \frac{\partial \underline{\underline{K}}_{fe}}{\partial \underline{X}} \underline{u}_e - \underline{\underline{K}}_{fe} \frac{\partial \underline{u}_e}{\partial \underline{X}} \right) \qquad 15$$

The linear finite element analysis is based on a Newtonian fluid resulting in a stiffness matrix and force vector that are independent of the solution variable, i.e.

$$\underline{\underline{K}} \neq \underline{\underline{K}}(\underline{X}), \quad {\partial \underline{\underline{K}}}/{\partial \underline{X}} = 0 \qquad \text{and} \qquad \underline{F}_f \neq \underline{F}_f(\underline{X}), \quad {\partial \underline{F}_f}/{\partial \underline{X}} = 0$$

such that Equation *14* reduces to

$$\frac{\partial \underline{F}_e}{\partial \underline{X}} = \left(\underline{\underline{K}}_{ee} - \underline{\underline{K}}_{ef} \underline{\underline{K}}_{ff}^{-1} \underline{\underline{K}}_{fe} \right) \frac{\partial \underline{u}_e}{\partial \underline{X}} \qquad 16$$

At each stage, we begin the process with an initial guess value for the fiber's velocity vector $\underline{X}^0$ and iteratively determine $\underline{X}$ using the Newton Raphson method in Equation 12, that results in a zero residual $\underline{R}$ solved for at each iteration based on the FEA algorithm. The iteration process is terminated when a desired error $\epsilon_d = |\underline{R}^+ - \underline{R}^-|$ criterion is satisfied.

We use an explicit fourth order Runge-Kutta (RK4) numerical scheme to track the fibers evolution and update the fiber's position (x_c^i, y_c^i) and orientation angle ϕ^i at each ith time step starting with an initial position (x_c^0, y_c^0) and orientation ϕ^0 [11], updating the input values of the responses obtained from the macro model at each RK4 stage when solving the for the fiber's velocities. Likewise, we update at each ith step, the geometry's mesh (nodal coordinate's) for a particular fiber position (x_c^i, y_c^i) and orientation, ϕ^i, according to the equation

$$\begin{bmatrix} x^i \\ y^i \end{bmatrix} = \begin{bmatrix} x_c^i \\ y_c^i \end{bmatrix} + \begin{bmatrix} \cos \phi^i & -\sin \phi^i \\ \sin \phi^i & \cos \phi^i \end{bmatrix} \begin{bmatrix} x_0^i \\ y_0^i \end{bmatrix}$$

Model Verification

Model validation of the micro-scale algorithm was performed in a 2-step process for an ellipsoidal fiber translating and rotating in simple shear flow with an initial fiber position $x_c^0 = y_c^0 = 0 \ mm$, and orientation angle $\phi^0 = 0 \ rad$. The velocity distribution of the undisturbed fluid motion employed in the validation was $U_{BC1} = \underline{U}_0' = \{0 \quad 0 \quad \dot{\gamma}y\}$ with, $\dot{\gamma} = 1s^{-1}$ and a far field pressure $p_{BC2} = p_0' = 0$. A fiber aspect ratio of $r_e = a/b = 6$ was used and with a sufficiently large ratio of the fluid domain to fiber size $\varepsilon = 2h/a = 40 \gg 1$.

In the first step, we benchmark results of the orientation and angular velocities from the simulation with those obtained from well-established Jeffery's analytical solution [8]. Jeffery assumed a zero resultant force and couple on an ellipsoidal particle suspended in a simple shear, homogenous, incompressible, Newtonian laminar flow. Jeffery's analytical solution is based on the assumptions that the particle center translates with the same translational velocity as the undisturbed fluid at that location.

Our 2D analysis is restricted to in-plane motion reducing the unknown rotation to a single angle, $\phi(t)$ and its derivative, i.e., the angular velocity $\omega = \dot{\phi}$ given as

$$\phi(t) = \tan^{-1}\left(r_e \tan\frac{\dot{\gamma}t}{r_e + 1/r_e}\right) \qquad 17$$

$$\dot{\phi} = \frac{\dot{\gamma}}{r_e^2 + 1}[1 + (r_e^2 - 1)\cos^2\phi] \qquad 18$$

The Jeffery's period T for fiber tumbling motion is given as

$$T = \frac{2\pi}{\dot{\gamma}}[r_e + 1/r_e] \qquad 19$$

The justification for our 2D simplification is based on

- It accurately predicts Jeffery's orbit, and provides a bases for us to study pressure distribution on the fibers surface
- Despite its inability to account for out-of-plane fiber's rotation, it provides insight into the pressure response which indicates potential void nucleation sites.
- It enables us utilize input along streamlines from the 2D macro model within the flow of polymer melt through a large-scale polymer deposition additive manufacturing flow field.

Figure 7 shows good agreement between our simulation and Jeffery's analytical solution for orientation angle and angular velocity for one complete Jeffery's period in simple shear flow. The noticeable discrepancy is attributed to the discretization employed in the FEA model, which was chosen to obtain the best solution at minimal computational cost.
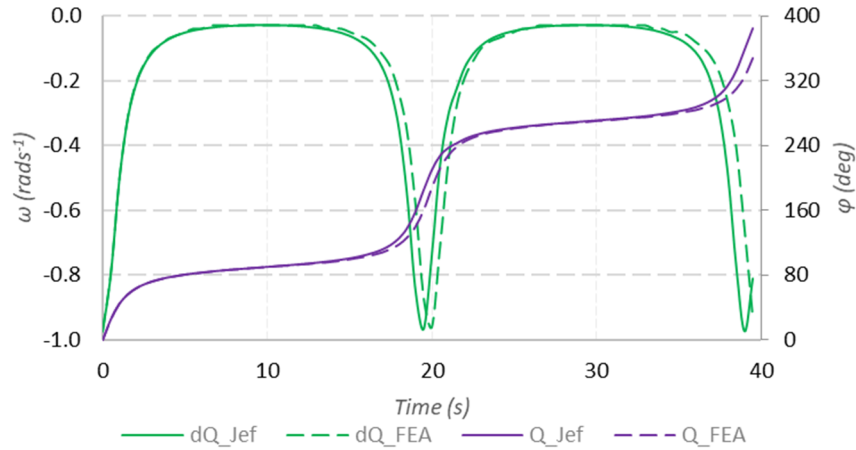

Figure 7: Fiber's angular velocity (green) and orientation angle (purple) for both Custom FEA code (dashed) and Jeffery's Solution (straight)

The maximum and minimum pressure near the fiber rotating in simple shear flow appears in Figure 8. As seen here, the minimum pressure around the fiber surface drops to a low point near -5kPa at the fiber's edge relative to the far field pressure of 0kPa. As such, the fiber experiences significant low pressure drops along it surface as it travels through Jeffery's orbit which suggests the likelihood of potential void nucleation at these low-pressure sites.
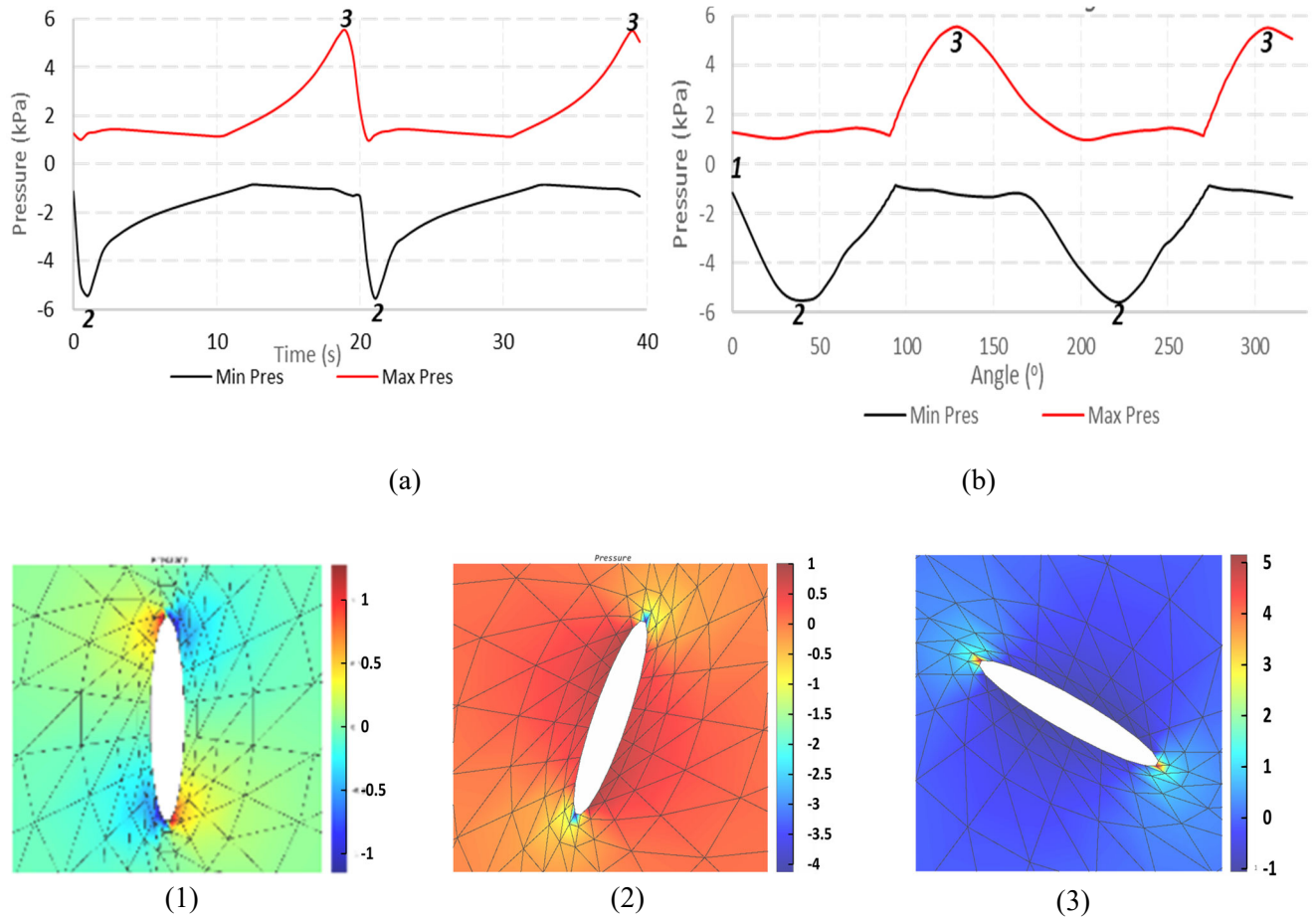
(a)

(b)

(1)

(2)

(3)

Figure 8: Minimum and maximum pressure profiles on the fiber's surface plotted against (a) time (b) fiber angle and pressure contours at indicated plot positions 1), 2), &3).

In the second step, we compare the velocity and pressure distributions computed from the custom FEA simulation to values calculated from a similar model developed in COMSOL Multiphysics for the initial fiber position and orientation (not shown here). Using similar discretization, triangle element type with quadratic order for both analysis we adopt an unbiased seed of 10 radial unit cell and 20 circumferential unit cells leading to a total of 400 elements for the entire domain. The discrepancy in both responses were seen to be only less than an order of 1%.

Results & Discussion

The fiber aspect ratio plays an important role in the pressure distribution on the fiber surface as it travels through Jeffery's orbit. Using simple shear flow conditions as described above, the pressure distribution for two aspect ratios were consideration $r_e = 3$ & $r_e = 6$. ; (b) $re = 3$;(a) $r_e = 6$,

shows that the pressure drop is more significant for higher aspect ratio ellipsoids. The shorter fibers tumble faster with a period $T_3 \approx 1/1.85 \ T_6$ due to a shorter dwell time as its axis comes into and out of alignment with the flow direction. The maximum rotational velocity occurs as the geometry becomes

spherical when $r_e = 1$ with a period $T_1 \approx 3/5 \ T_3$, which also has no significant pressure variation during rotation.   (a)   (b)

Figure 11 shows the results for 2 different shear rates, $\dot{\gamma} = 1 \ \& \ 2 s^{-1}$ with other factors being constant. Computed results show that a higher rotational velocity occurs under higher shear rates, as expected. The minimum and maximum pressure appearing in Figure 11 also shows a greater drop in minimum pressure value as the velocity gradient increases. Overall, these simple shear flow results show that a higher velocity gradient and aspect ratio generate lower minimum melt pressures which is expected to be more likely to form voids which is consistent with conclusion drawn from [6].
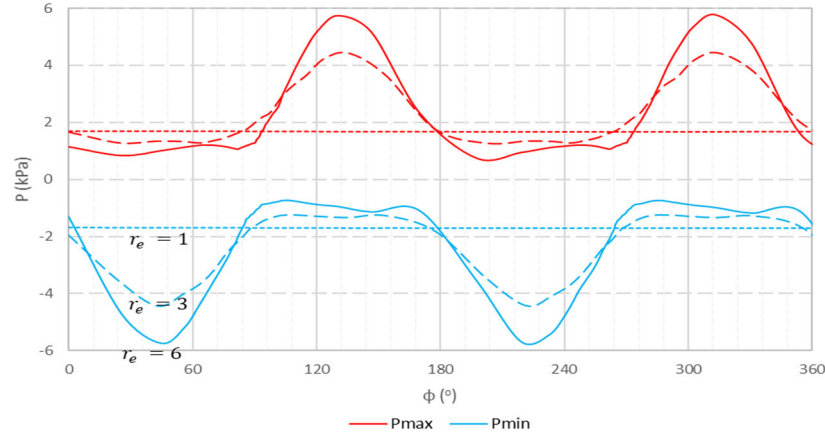

Figure 9: Minimum and maximum pressure profiles for various aspect ratio ($r_e = 1, 3, 6$)
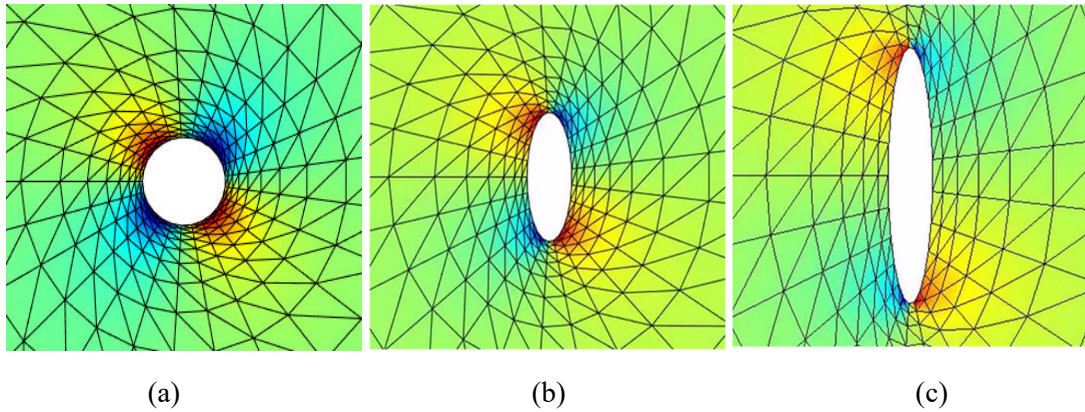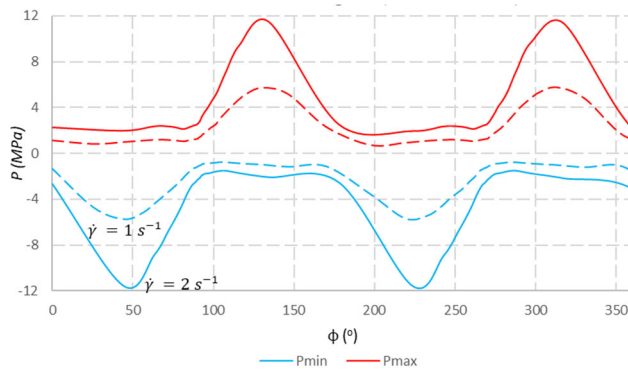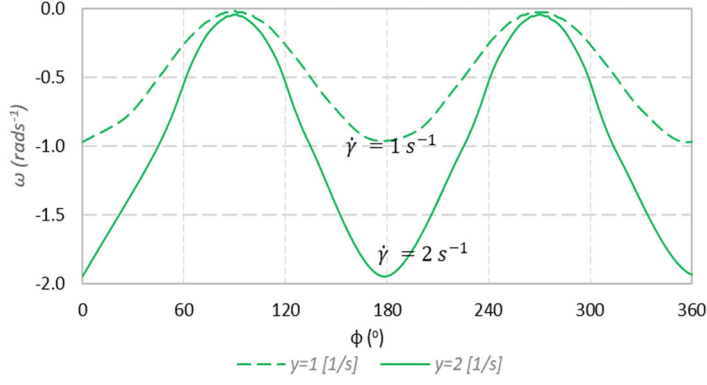

(a)   (b)   (c)

Figure 10: Pressure Distribution around fiber surface (a) $r_e = 1$; (b) $r_e = 3$;(a) $r_e = 6$,

(a)   (b)

Figure 11:Results for different shear rates ($\dot{\gamma} = 1 \,\&\, 2s^{-1}$) (a) Min. and max Pressure (b) Angular velocity

The results presented above are based on a constant shear rate flow field. For subsequent analyses, we present simulation results for a fiber traveling through the extrusion deposition flow and use the pressure, velocity and velocity gradients along select streamlines ($\psi_{10}, \psi_{15}, \psi_{18}$) from the 2D planar BAAM nozzle deposition flow simulations described above appearing in Figure 12.
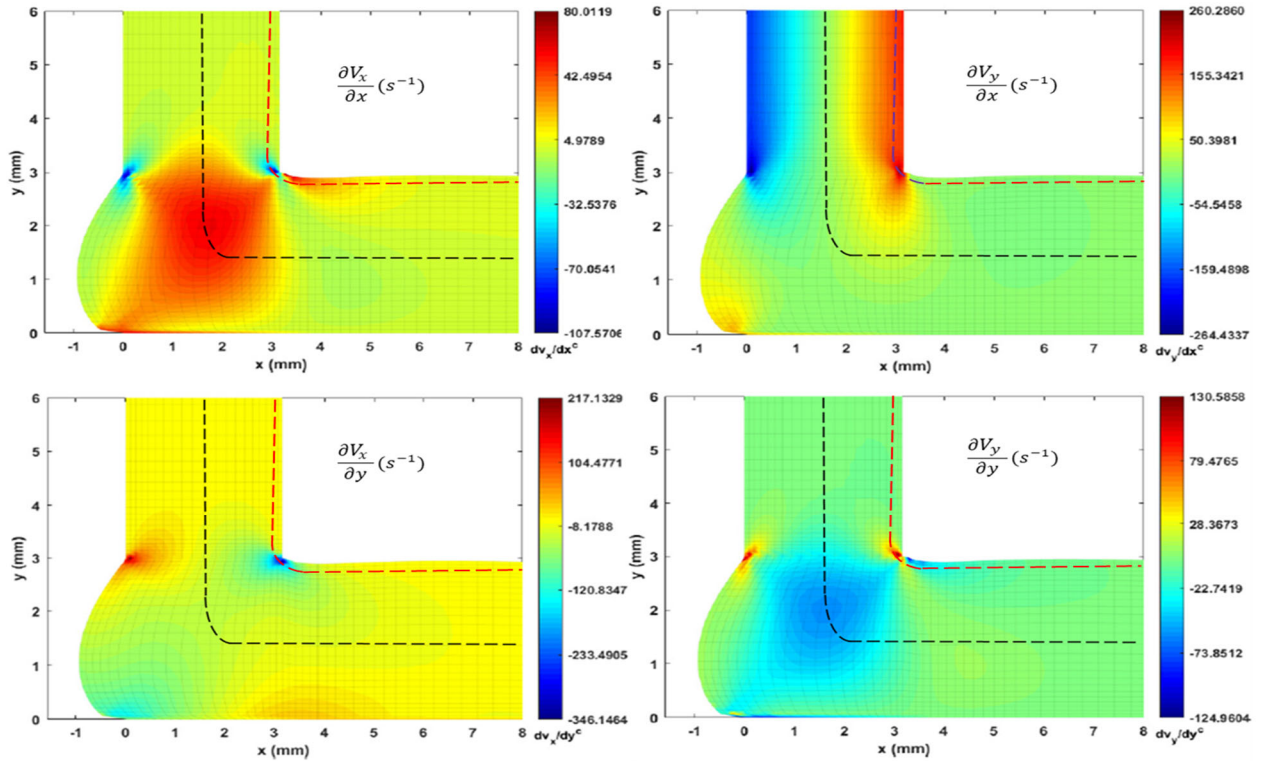

Figure 12: Velocity gradient contours near extrusion-deposition transition - $\partial v_x/\partial x$ (top-left), $\partial v_y/\partial x$ (top-right), $\partial v_x/\partial y$ (bottom-left), $\partial v_y/\partial y$ (bottom-right)

Velocity gradients computed in the macro scale simulation (cf. Figure 12) shows that the dominant gradient is the vertical shear component $-\partial v_y/\partial x$ which increases radially outward from the centerline towards the outside of the nozzle, i.e., the velocity gradients increase between streamline 10 to streamline 18. Velocity contours in Figure 12 also expose the singularity at the edge of the nozzle where the polymer melt flow transitions from a no-slip to a free surface boundary condition. After the melt leaves the nozzle and turns onto the plate, it has a uniform velocity, and the shear rates go to zero.

Figure 13 shows the relative increase in shear rates at the nozzle exit from the center streamline to streamlines closer to the nozzle edge. As the fiber moves along the center streamline from the inlet through the nozzle to the bed fiber rotation is relatively low (about 45°) due to the low velocity gradient as compared to streamlines closer to the edge that have much higher gradients (about 170° for ψ_{15} and 290° for ψ_{18}).
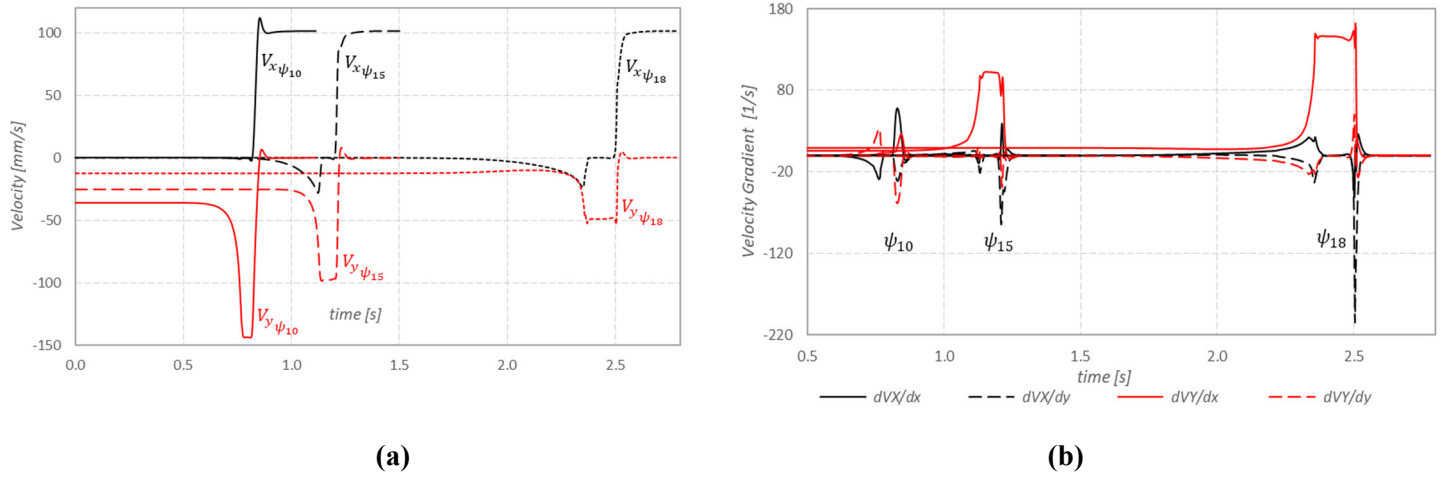

(a)   **(b)**

Figure 13: (a) Streamline velocities ($\psi_{10}, \psi_{15}, \psi_{18}$), (b) Velocity gradients ($\psi_{10}, \psi_{15}, \psi_{18}$),
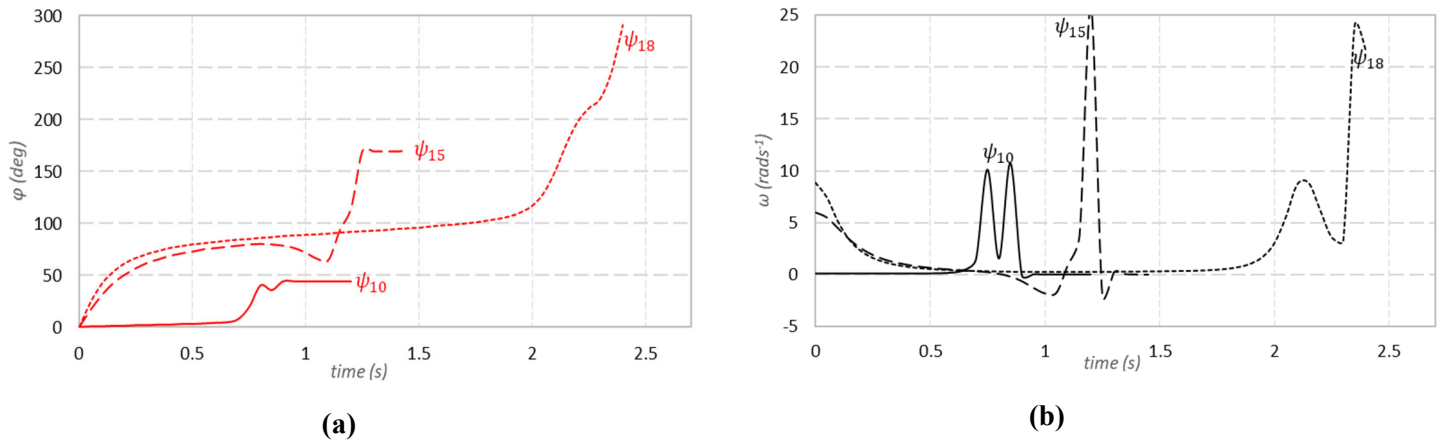

(a)   **(b)**

Figure 14: (a) Fiber's orientation angle ($\psi_{10}, \psi_{15}, \psi_{18}$), (b) Fiber's angular velocity ($\psi_{10}, \psi_{15}, \psi_{18}$),

The minimum pressure drop on the fiber's surface at the nozzle exit is seen to be higher for the center streamline as compared to those farther away as we see in Figure 15where the minimum pressure on streamline ψ_{10} drops to about -0.5MPa pressure, whereas for streamline ψ_{15} though minimum pressure

stays beneath the far field pressure, the drop is just about 0.8MPa gauge pressure and almost no noticeable dip on streamline ψ_{18} which is very near the nozzle's edge. The micro-model solution along streamline 18 exhibits numerical instability near 2.4sec where the polymer exits the nozzle due to singularities in the macro-model velocity solution at this point. Additional work is needed to fully understand the effect of the singularity.
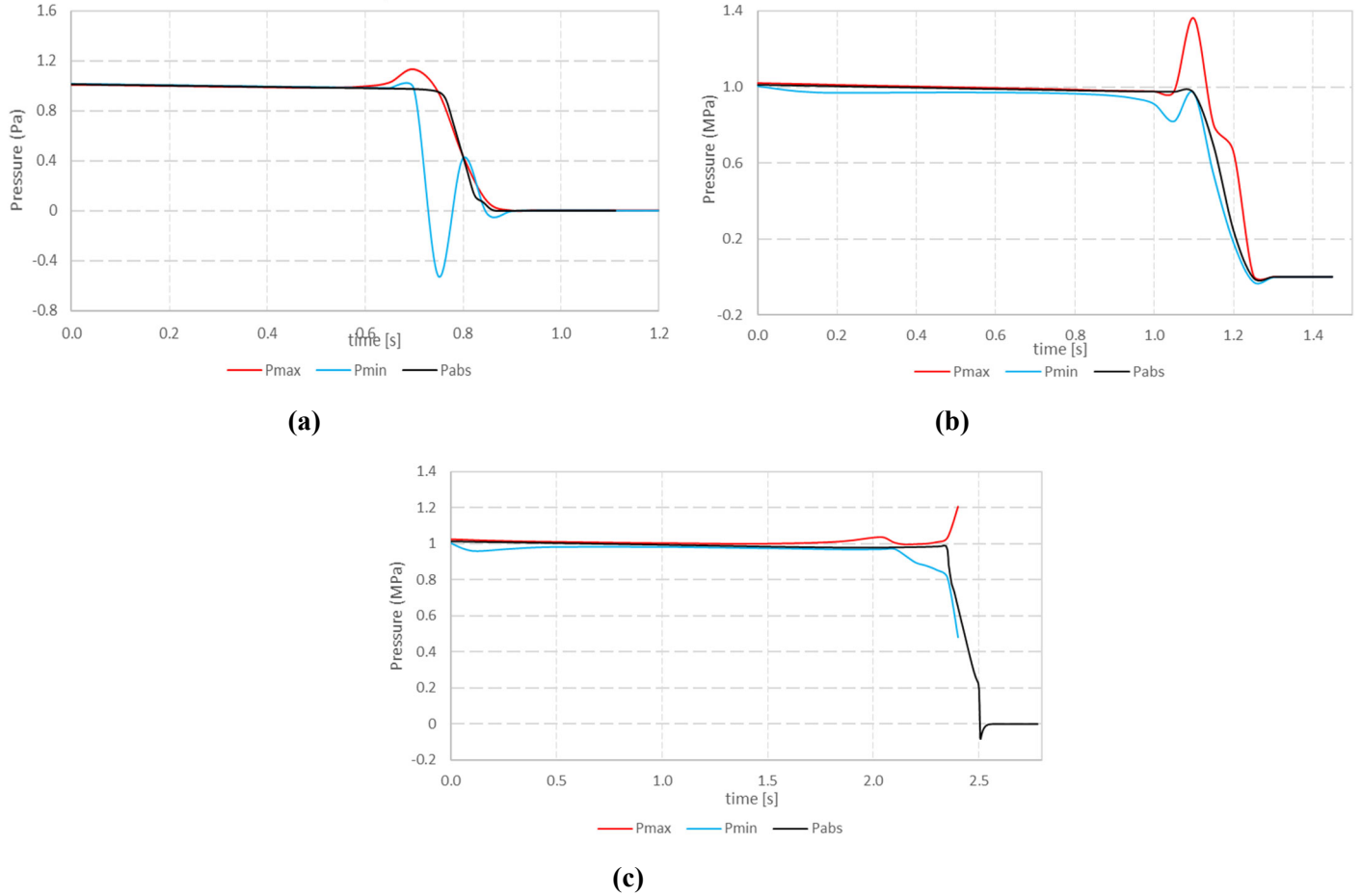

(a)

(b)

(c)

Figure 15: (a) (b) (c), Minimum, maximum and streamline pressure for Streamline - ψ_{10}, ψ_{15},& ψ_{18} respectively

Conclusion

In conclusion, we have successfully developed and implemented a multiscale approach for predicting fiber motion and fluid pressure around a single suspended fiber in polymer composite deposition flow. Computed results show that the single fiber model accurately predicts Jeffrey's orbit in simple shear flow and provides expected trends as the aspect ratio and shear-rates are increased. Also, the results show significant minimum pressure on the fiber surface during BAAM polymer composite deposition, which is seen to be streamline dependent, and serves as pointers that indicate the likelihood of void formation near fibers in BAAM deposition flow.

As a future endeavor, we plan to extend the multi-scale modeling approach to 3D flow simulation and investigate the effect of other geometry and flow parameters on minimum pressure prediction. We also plan to develop a relationship between print processing parameters and likelihood of void formation, implement a generalize Newtonian fluid model in the nozzle flow and single fiber model and establish a relationship between minimum pressures and void initiation.

References

1.   Rajaguru, K., Karthikeyan, T. and Vijayan, V., 2020. Additive manufacturing–State of art. Materials today: proceedings, 21, pp.628-633.
2.   Van de Werken, N., Tekinalp, H., Khanbolouki, P., Ozcan, S., Williams, A. and Tehrani, M., 2020. Additively manufactured carbon fiber-reinforced composites: State of the art and perspective. Additive Manufacturing, 31, p.100962.
3.   Mehdikhani, M., Gorbatikh, L., Verpoest, I. and Lomov, S.V., 2019. Voids in fiber-reinforced polymer composites: A review on their formation, characteristics, and effects on mechanical performance. Journal of Composite Materials, 53(12), pp.1579-1669.
4.   Heller, B.P., Smith, D.E. and Jack, D.A., 2019. Planar deposition flow modeling of fiber filled composites in large area additive manufacturing. Additive Manufacturing, 25, pp.227-238.
5.   Wang, Z., 2019. Computational Modeling of Fiber Reinforced Composites Melt Flow in Nozzle Extrudate for Polymer Deposition Additive Manufacturing (Doctoral dissertation, Baylor University).
6.   Vaxman, A., Narkis, M., Siegmann, A. and Kenig, S., 1989. Void formation in short-fiber thermoplastic composites. Polymer composites, 10(6), pp.449-453.
7.   Yang, D., Zhang, H., Wu, J. and McCarthy, E.D., 2021. Fibre flow and void formation in 3D printing of short-fibre reinforced thermoplastic composites: An experimental benchmark exercise. Additive Manufacturing, 37, p.101686.
8.   Jeffery, G. B. The motion of ellipsoidal particles immersed in a viscous fluid. Proceedings of the Royal Society of London. Series A, 102(715):161-179, 1922.
9.   Wang, Z. and Smith, D.E., 2021. A Fully Coupled Simulation of Planar Deposition Flow and Fiber Orientation in Polymer Composites Additive Manufacturing. Materials, 14(10), p.2596.
10.   Zhang, D. and Smith, D.E., 2016. Dynamic simulation of discrete fiber motion in fiber-reinforced composite materials processing. Journal of Composite Materials, 50(10), pp.1301-1319.
11.   Zhang, D. and Smith, D.E., 2015. Finite element-based brownian dynamics simulation of nanofiber suspensions using Monte Carlo Method. Journal of Micro and Nano-Manufacturing, 3(4).
12.   Fallon, J.J., McKnight, S.H. and Bortner, M.J., 2019. Highly loaded fiber filled polymers for material extrusion: A review of current understanding. Additive Manufacturing, 30, p.100810.
13.   Reddy, J.N., 2019. Introduction to the finite element method. McGraw-Hill Education.